



# Coordination of a Single Calcium Ion in the EF-hand Maintains the Off State of the Stromal Interaction Molecule Luminal Domain

Masahiro Enomoto<sup>1,\*</sup>, Tadateru Nishikawa<sup>1,\*†</sup>, Sung-In Back<sup>1</sup>, Noboru Ishiyama<sup>1,‡</sup>, Le Zheng<sup>1</sup>, Peter B. Stathopoulos<sup>2</sup> and Mitsuhiko Ikura<sup>1</sup>

**1** - Princess Margaret Cancer Centre, Department of Medical Biophysics, University Health Network, University of Toronto, Toronto, ON M5G 1L7, Canada

**2** - Department of Physiology and Pharmacology, Schulich School of Medicine and Dentistry, London, ON, Canada N6A 5C1

**Correspondence to** Mitsuhiko Ikura and Peter B. Stathopoulos: [pstatho@uwo.ca](mailto:pstatho@uwo.ca), [mikura@uhnresearch.ca](mailto:mikura@uhnresearch.ca)

<https://doi.org/10.1016/j.jmb.2019.10.003>

**Edited by Ichio Shimada**

## Abstract

Store operated calcium ( $\text{Ca}^{2+}$ ) entry (SOCE) is the process whereby endoplasmic reticulum (ER)  $\text{Ca}^{2+}$  store depletion causes Orai1-composed  $\text{Ca}^{2+}$  channels on the plasma membrane (PM) to open, mediating a rise in cytosolic  $\text{Ca}^{2+}$  levels. Stromal interaction molecules (STIMs) are the proteins that directly sense ER  $\text{Ca}^{2+}$  content and gate Orai1 channels due to store depletion. The trigger for STIM activation is  $\text{Ca}^{2+}$  unbinding from the ER lumen-oriented domains, which consist of a nonconserved amino (N) terminal region and EF-hand and sterile  $\alpha$  motif (SAM) domains (EF-SAM), highly conserved from humans to *Caenorhabditis elegans*. Solution NMR structures of the human EF-SAM domains have been determined at high  $\text{Ca}^{2+}$  concentrations; however, no direct structural view of the  $\text{Ca}^{2+}$  binding mode has been elucidated. Further, no atomic resolution data currently exists on EF-SAM at low  $\text{Ca}^{2+}$  levels. Here, we determined the X-ray crystal structure of the *C. elegans* STIM luminal domain, revealing that EF-SAM binds a single  $\text{Ca}^{2+}$  ion with pentagonal bipyramidal geometry and an ancillary  $\alpha$ -helix formed by the N-terminal region acts as a brace to stabilize EF-SAM. Using solution NMR, we observed EF-hand domain unfolding and a conformational exchange between folded and unfolded states involving the ancillary  $\alpha$ -helix and the canonical EF-hand in low  $\text{Ca}^{2+}$ . Remarkably, we also detected an  $\alpha$ -helix ( $+\text{Ca}^{2+}$ ) to  $\beta$ -strand ( $-\text{Ca}^{2+}$ ) transition at the terminal SAM domain  $\alpha$ -helix. Collectively, our analyses indicate that one canonically bound  $\text{Ca}^{2+}$  ion is sufficient to stabilize the quiescent luminal domain structure, precluding unfolding, conformational exchange, and secondary structure transformation.

© 2019 Elsevier Ltd. All rights reserved.

Store operated calcium ( $\text{Ca}^{2+}$ ) entry (SOCE) is a fundamental cell signaling process used by all eukaryotes. SOCE occurs when the major intracellular endoplasmic reticulum (ER)  $\text{Ca}^{2+}$  store becomes depleted, which leads to opening of highly  $\text{Ca}^{2+}$ -selective channels on the plasma membrane (PM) that allow movement of  $\text{Ca}^{2+}$  down the steep concentration gradient from the extracellular space into the cytosol [1–3]. Free cytosolic  $\text{Ca}^{2+}$  concentrations can increase by as much as ~10-fold from ~0.1  $\mu\text{M}$  to ~1  $\mu\text{M}$  due to SOCE, signaling a plethora of vital processes central to life and death and providing a source of  $\text{Ca}^{2+}$  for refilling the ER and other intracellular stores [4,5].

The protein machinery that predominantly mediates SOCE includes the stromal interaction molecule (STIM) [6–8] and the Orai proteins [9–13]. The Orai proteins assemble as hexamers to form  $\text{Ca}^{2+}$ -selective channels on the PM [14]. The STIMs are ER-resident proteins with functional domains located in the cytosol and ER lumen. Humans and other vertebrates express two STIM (i.e., STIM1 and STIM2) [15] and three Orai paralogs (i.e., Orai1, Orai2, Orai3) [16]. Orai1 homomers form  $\text{Ca}^{2+}$  release activate  $\text{Ca}^{2+}$  (CRAC) channels that mediate a majority of the SOCE in most cell types. Orai2 and Orai3 may have more tissue-specific roles [2].

In nonexcitable cells, SOCE can be stimulated downstream of any cell surface G protein-coupled receptor (GPCR) activation that results in inositol 1,4,5-trisphosphate ( $\text{IP}_3$ ) production and  $\text{IP}_3$  receptor channel opening on the ER, depleting ER  $\text{Ca}^{2+}$  levels. However, any mode of ER  $\text{Ca}^{2+}$  depletion will stimulate SOCE. STIMs contain EF-hand and sterile  $\alpha$ -motif (SAM) domains oriented in the ER lumen and a series of coiled-coil domains in the cytosol [17,18]. These luminal and cytosolic domains have a high-sequence similarity among STIM orthologs [15]. A single pass transmembrane (TM) domain separates the luminal from the cytosolic conserved domains.

STIM1 forms dimers on the ER membrane due to interactions by the cytosolic coiled-coil domains [19–24]. These inactive STIM1 dimers pervasively diffuse along the ER [25]. When the ER  $\text{Ca}^{2+}$  stores are full, the luminal domains remain monomeric due to  $\text{Ca}^{2+}$ -binding dependent stabilization of the EF-hand and SAM domain (EF–SAM) intramolecular interaction [26–29]. When the ER  $\text{Ca}^{2+}$  stores are depleted, this luminal intramolecular interaction is destabilized, leading to EF–SAM dimerization [26,27,30–32]. This EF–SAM dimerization induces a marked conformational rearrangement of the cytosolic coiled-coils [19,24,33] that leads to trapping of activated STIM1 molecules at ER-PM junctions [25,34]. The trapping of STIM1 occurs due to a release of a polybasic C-terminal region of STIM1 that affords interactions with PM phosphoinositides [35–38] and due to direct interactions by the STIM1 coiled-coils with Orai1 protein subunits [39,40]. These direct STIM1–Orai1 interactions gate the Orai1 channels.

High-resolution structures of the human STIM1 and STIM2 EF–SAM have been determined by solution NMR only in a high molar excess of  $\text{Ca}^{2+}$  (high  $\text{Ca}^{2+}$ ) [27,29]. However, distance restraints coordinating  $\text{Ca}^{2+}$  were not directly determined in these structures. Furthermore, these human structures lacked the variable N-terminal regions shown to play a modulatory role in the  $\text{Ca}^{2+}$  sensing mechanism of STIM1 and STIM2 [32,41,42]. Therefore, the precise mechanism of  $\text{Ca}^{2+}$  coordination, how the variable N-terminal region of STIMs affect core EF–SAM structure, and mechanism of STIM luminal domain dimerization in buffer nominally free of  $\text{Ca}^{2+}$  (low  $\text{Ca}^{2+}$ ) remain major knowledge gaps in the field.

Here, we present the crystal structure of the *Caenorhabditis elegans* STIM (cSTIM) luminal domain in the presence of high  $\text{Ca}^{2+}$ , revealing a single  $\text{Ca}^{2+}$  ion coordinated in the canonical EF-hand loop with pentagonal bipyramidal geometry and that the nonconserved N-terminal region forms an ancillary  $\alpha$ -helix that further stabilizes the core EF–SAM structure. In addition, we used solution NMR to probe the structure and folding of this *C. elegans* luminal domain in low  $\text{Ca}^{2+}$ , discovering

that the EF-hand and ancillary  $\alpha$ -helices are in conformational exchange between folded and unfolded states. Finally, our NMR data show that the C-terminal helix of the luminal SAM domain, which is intimately involved in maintaining the intramolecular EF-hand:SAM domain interaction in the presence of high  $\text{Ca}^{2+}$ , undergoes a remarkable  $\alpha$ -helix to  $\beta$ -strand transition in low  $\text{Ca}^{2+}$ . Collectively, our crystal and solution NMR data provide previously unappreciated atomic level insights into the mechanisms underlying STIM activation.

## Results

### *C. elegans* EF–SAM is structurally similar to human STIM2 EF–SAM

In high  $\text{Ca}^{2+}$ , the human STIM1 and STIM2 EF-hand and SAM domains fold into a combined compact structure made up of ten  $\alpha$ -helices and two short  $\beta$ -strands [27,29]. The EF-hand domain of each human paralog consists of four  $\alpha$ -helices and two loops, whereas the SAM domain adopts a compact five-helix bundle. In the  $\text{Ca}^{2+}$ -bound state, the terminal SAM helix (i.e.,  $\alpha_{10}$ ) packs into a hydrophobic cleft made up of the two EF-hand motifs, thereby promoting the overall compact configuration. This conformation is further buttressed via the small  $\beta$ -sheet formed by backbone hydrogen (H) bonding between loop I and II of the EF-hand motifs.

Here, our *C. elegans* crystal structure (1.89 Å resolution) reveals the EF–SAM region of this lower eukaryotic STIM conserves these characteristic features central to regulating the activation state of the molecule and SOCE (Fig. 1A). The crystal structure determined in high  $\text{Ca}^{2+}$  shows a canonical helix–loop–helix motif ( $\alpha_1–\beta_1–\alpha_2$ ). Immediately downstream of the canonical EF-hand motif is a second helix–loop–helix motif ( $\alpha_3–\beta_2–\alpha_4$ ), which pairs with the first EF-hand through backbone H-bonding between  $\beta_1$  and  $\beta_2$ , forming a short  $\beta$ -sheet. The second, noncanonical EF-hand loop is not clearly identifiable based on primary structure for neither the human STIMs nor *C. elegans* (Fig. 1B). A short linker helix ( $\alpha_5$ ) links the *C. elegans* EF-hand domain in sequence space to the five-helix bundle-composed SAM domain ( $\alpha_6–\alpha_{10}$ ). This SAM domain alone buries 13 residues that are at least 85% solvent inaccessible (Fig. S1).

The EF-hand and SAM domains of the *C. elegans* STIM form intimate contacts, primarily mediated by nonpolar interactions. In high  $\text{Ca}^{2+}$ , these intimate EF-hand:SAM hydrophobic interactions are a hallmark feature of STIM  $\text{Ca}^{2+}$  sensing that supports a quiescent conformation [27]. In *C. elegans* STIM, the EF-hand domain forms a hydrophobic cleft made up

of at least 13 residues with nonpolar character (Fig. 1C). This extensive hydrophobic pocket serves as a docking site for the hydrophobic L176 and L180 anchor residues found on the  $\alpha$ 10 helix of the SAM domain (Fig. 1D). In *C. elegans*, the EF-hand:SAM domain interaction is reinforced through one ionic bond involving R85 within  $\alpha$ 3 of the noncanonical EF-hand motif and D177 within  $\alpha$ 10 of the SAM domain (Fig. 1E). These hydrophobic and ionic interactions pull the SAM domain of *C. elegans* STIM into the EF-hand cleft and promote a compact globular fold.

Despite the continuity in global structure of cSTIM EF–SAM, the electrostatic surface potential is separable based on domain. A highly negative surface potential is apparent over the EF-hand domain, whereas the closely packed SAM domain is slightly electropositive (Fig. 1F). These domain differences in surface potential are exacerbated further when removing the positive charge contribution of the  $\text{Ca}^{2+}$  ion from the calculation. The strongly negative surface potential of the EF-hand domain is consistent with a role in the electrostatic guidance of free  $\text{Ca}^{2+}$  into the canonical binding loop, which is preserved throughout evolution from *C. elegans* to humans.

Within the EF-hand domain cleft, the *C. elegans* SAM domain is rotated away from the canonical EF-hand motif such that the  $\alpha$ 2 of the canonical EF-hand adopts a nearly parallel orientation relative to the  $\alpha$ 10 helix of the SAM domain (i.e.,  $\sim 155^\circ$   $\alpha$ 2– $\alpha$ 10 interhelical angle; Fig. 2A). This geometry is remarkably similar to that observed for the human STIM2 solution EF–SAM structure in high  $\text{Ca}^{2+}$  (i.e.,  $\sim 150^\circ$   $\alpha$ 2– $\alpha$ 10 interhelical angle), but distinct from the nearly perpendicular orientation observed for human STIM1 EF–SAM in high  $\text{Ca}^{2+}$  (i.e.,  $\sim 94^\circ$   $\alpha$ 2– $\alpha$ 10 interhelical angle; Fig. 2B and C) [29]. To accommodate this orientation, both the *C. elegans* and the human STIM2 EF-hand clefts are expanded (i.e., 13 residues) compared with human STIM1 (i.e., 11 residues); however, the mechanism of the cleft expansion appears to be distinct for *C. elegans* compared with human STIM2. In human STIM2, W128 and K103 point into the cleft compared with the aligned residues in human STIM1 (i.e., W124 and H99), which are directed away; moreover, the equivalent *C. elegans* residues (i.e., W105 and R78) are directed away from the cleft similar to STIM1, yet the total number of residues contributing to the cleft is similar to STIM2 due to the unique inclusion of M71 and M77 by *C. elegans* EF–SAM (Fig. 1C) [29].

### *C. elegans* EF–SAM coordinates one $\text{Ca}^2$ ion located in the canonical EF-hand loop

The present *C. elegans* crystal structure provides the first direct atomic-level view into the mode of

$\text{Ca}^{2+}$  binding to the luminal domain of any STIM protein. Examination of the  $F_o - F_c$  electron density map contoured at  $2.0\sigma$  shows only a single location of high electron density outside the polypeptide chain that could be attributable to  $\text{Ca}^{2+}$ , despite the relatively high  $\text{CaCl}_2$  concentration (i.e., 10 mM) used for crystallization (Fig. 3A). The coordination of  $\text{Ca}^{2+}$  within the canonical EF-hand loop occurs with pentagonal bipyramidal geometry as observed for calmodulin, parvalbumin, and other EF-hand proteins (Fig. 3A) [43,44]. The residues involved in  $\text{Ca}^{2+}$  binding within the 12-residue canonical EF-hand loop are D55 ( $\text{O}\delta 1$ , position X), D57 ( $\text{O}\delta 1$ , position Y), S59 ( $\text{O}\gamma$ , position Z), S61 (backbone CO, position #), D63 ( $\text{O}\delta 2$ , position y), and E66 ( $\text{O}\epsilon 1$  and  $\text{O}\epsilon 2$ , position z). Whereas positions X, Y, and Z provide a single ligand for  $\text{Ca}^{2+}$  binding via side chain oxygen atoms, position # contributes to the coordination via a backbone carbonyl oxygen, position y bridges a first coordination shell water molecule through a side chain oxygen atom, and position z provides a bidentate ligand through both side chain oxygen atoms. All seven first coordination shell oxygen ligands are within  $2.5 \text{ \AA}$  of the  $\text{Ca}^{2+}$  ion (Fig. 3A).

The Glu at position z (i.e., 12th residue) in the canonical EF-hand loop is critical for the observed pentagonal bipyramidal geometry due to the side chain length and bidentate contribution to the coordination. In other canonical EF-hand containing proteins, when this z position is occupied by Asp, which also has a side chain carboxylate group with two oxygen atoms available for bidentate coordination but has a shorter side chain compared with Glu,  $\text{Ca}^{2+}$  is coordinated with octahedral geometry and a preference for  $\text{Mg}^{2+}$  is observed [45,46]. In other canonical EF-hand containing proteins, substitution of the Glu in this z position with Gln, which has a side chain of the same length but provides only one oxygen atom for coordination (monodentate),  $\text{Ca}^{2+}$  binding affinity is reduced [47,48]. We note that the Glu at position z is highly conserved in the canonical EF-hand of STIMs from higher and lower order organisms [15].

To assess more judiciously the number of possible  $\text{Ca}^{2+}$  binding sites within the entire luminal domain, we calculated the  $F_o - F_c$  omit map for the dimeric asymmetric unit after removal of the  $\text{Ca}^{2+}$  ion from the structure. A series of  $F_o - F_c$  omit map views contoured at  $2.0, 4.0, 6.0, 8.0$ , and  $16.0\sigma$  shows a strong unaccounted-for electron density only in the canonical EF-hand loop, which is persistent through all contour levels shown (Fig. S2A–E). A closer comparison of the omit map in the EF-hand loops reinforces the unaccounted-for electron density in the canonical EF-hand loop contoured at  $9.0\sigma$  (Fig. 3A), but not the noncanonical EF-hand loop contoured at  $9.0\sigma$  or  $2.0\sigma$  (Fig. 3B). Thus, *C. elegans* STIM EF–SAM stably coordinates only one  $\text{Ca}^{2+}$  ion.

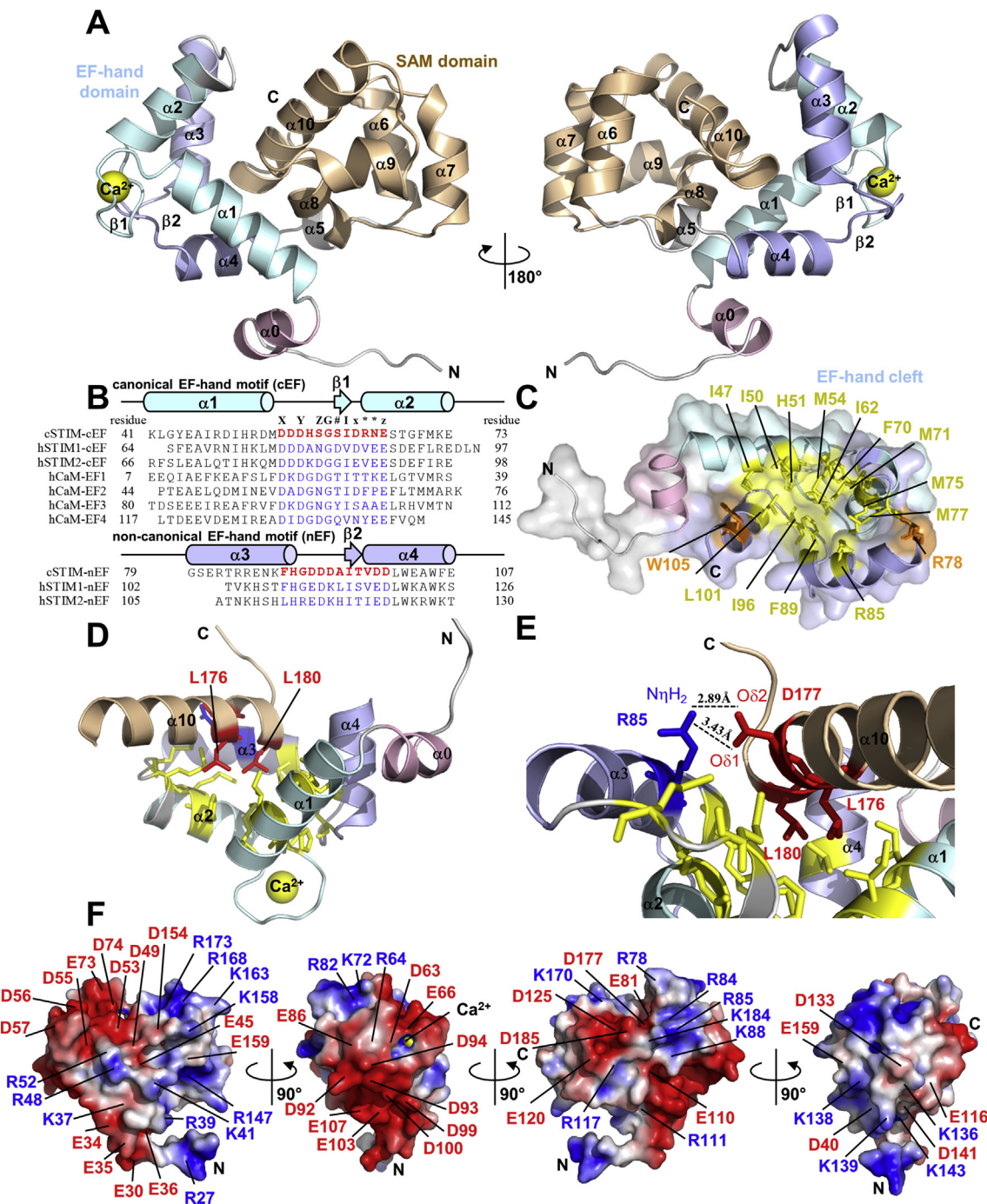


**Fig. 1.** X-ray crystal structure features of  $\text{Ca}^{2+}$ -bound *Caenorhabditis elegans* STIM luminal domain. (A) Cartoon view of the EF–SAM structural fold in the context of the full *C. elegans* luminal domain (cSTIM–L<sub>full</sub>). The SAM domain (brown) docks into a cleft formed by the canonical EF-hand (cyan) and noncanonical EF-hand (light blue) motifs. The EF-hand and SAM domains are linked by the  $\alpha$ 5 helix (gray). An ancillary  $\alpha$ 0 helix (pink) in the variable N-terminal region is visible. Individual secondary structure components are labeled. (B) Sequence alignment of canonical and noncanonical EF-hand motifs of human and *C. elegans* STIMs. The secondary structure components of the motifs based on the X-ray crystal structure of cSTIM–L<sub>full</sub> are shown above the sequences. The four EF-hand motifs of human calmodulin (hCaM) are shown for comparison. The 12-residue loop of *C. elegans* STIM are colored red, whereas human STIM1 (hSTIM1), STIM2 (hSTIM2), and hCaM are colored blue. The residues involved in coordination (X, Y, Z, #, x, and z) and the invariant G and I residues are indicated above the loop sequence. The residue ranges are shown at left and right of each sequence based on the accession numbers shown in Table 1 and AAD45181.1 for hCaM. (C) Surface and cartoon view of the EF-hand cleft formed by *C. elegans* STIM. The 13 cleft forming residues are labeled and shown as yellow sticks. The residues that are

### The variable N-terminal region of *C. elegans* STIM forms an ancillary $\alpha$ -helix that interacts with both the EF-hand and SAM domains

An isolated peptide derived from the human STIM1 nonconserved N-terminal region (i.e., residues 24–57), upstream of EF–SAM, remains unstructured in solution [49]; nevertheless, paramagnetic relaxation enhancement (PRE) NMR experiments suggest that this peptide interacts with the EF–SAM core near the W121 and K122 residues [42]. Here, our crystal structure of the *C. elegans* luminal STIM domains reveals the nonconserved N-terminal region forms a previously unseen  $\alpha$ -helix ( $\alpha_0$ ), upstream of the EF–SAM core (Fig. 4A). This  $\alpha_0$  helix is stabilized by an intrahelix ionic interaction between E36 and R39 (Fig. 4B). Further, this ancillary  $\alpha$ -helix contacts both the EF-hand and SAM domains of *C. elegans*. Specifically, the A33 carbonyl oxygen of  $\alpha_0$  is within 3.0 Å of the W102 indole N $\epsilon$ 1 atom of the EF-hand domain and the E36 O $\epsilon$ 2 atom is within 2.7 Å of the R111 guanidinium N $\eta$ 2 atom on the SAM domain (Fig. 4B). Remarkably, the W102 of the *C. elegans* EF–SAM is equivalent to the W121 position on human STIM1, which is the N-terminal region contact site identified on human STIM1 EF–SAM using PRE [42]. Thus, despite the lack of sequence conservation between the N-terminal regions of STIM homologues from higher to lower eukaryotes, interactions of these regions with the respective EF–SAM core may be a conserved structural feature among all STIM proteins.

### The nonconserved N-terminal region of *C. elegans* and human STIMs enhance the stability of the luminal domain

Destabilizing EF–SAM mutations constitutively activate full-length human STIM1 and SOCE [27]. Further, engineering superstable human STIM1/STIM2 EF–SAM chimeras into full-length STIM1 results in inhibited SOCE, whereas unstable EF–SAM chimeras constitutively activate SOCE [29]. In addition, stabilizing luminal domain post-translational modifications inhibit human STIM1 activation [42], whereas destabilizing modifications promote STIM1 activation and SOCE [50,51]. Having elucidated a previously unidentified  $\alpha_0$  helix in

the luminal domain of *C. elegans* STIM that contacts the EF–SAM core, and given the demonstrated importance of stability to human STIM1 activation, we then probed the effect of extending human STIM1 and human STIM2 EF–SAM constructs to include the respective variable N-terminal regions on stability. We created human STIM1 and STIM2 EF–SAM constructs that were extended N-terminally ( $N_{\text{ext}}$ ). Our *C. elegans* crystal structure construct encompassed all residues of the luminal domain ( $L_{\text{full}}$ ), already including both N- and C-terminal extensions relative to EF–SAM; thus, we created a *C. elegans* construct with a deleted nonconserved N-terminal region ( $L_{\Delta N}$ ).

Far UV circular dichroism (CD) spectra show that all proteins have enhanced  $\alpha$ -helicity in high  $\text{Ca}^{2+}$  compared with low  $\text{Ca}^{2+}$  (Fig. S3A–D). We monitored the change in far-UV CD signal at 225 nm as a function of increasing temperature as an indicator of stability. In high  $\text{Ca}^{2+}$  (i.e., 5 mM  $\text{CaCl}_2$ ), the thermal melts showed that the apparent midpoints of temperature denaturation ( $T_m$ ) of the cSTIM– $L_{\text{full}}$  was ~7.5 °C higher compared with the cSTIM– $L_{\Delta N}$  with the N-terminal deletion (Fig. S3E and F; Table 1). Consistent with a stabilizing role of the variable N-terminal region, the  $T_m$  values of human STIM1– $N_{\text{ext}}$  and STIM2– $N_{\text{ext}}$  were enhanced by ~15.5 and 11.5, respectively, compared with the EF–SAM cores alone (Fig. S3G and H; Table 1). A similar increase in thermal stability was observed under low  $\text{Ca}^{2+}$  conditions with the inclusion of the N-terminal regions stabilizing the human STIM1 and human STIM2 EF–SAM domains by ~15.5 and 14.0 °C, respectively, and deletion of the N-terminal region destabilizing the full cSTIM luminal domain by ~12.5 °C (Fig. S3E–H; Table 1). All proteins showed a dramatic decrease in  $T_m$  in low  $\text{Ca}^{2+}$  compared with high  $\text{Ca}^{2+}$  (i.e.,  $\Delta T_m$  ranging from ~11.5 to 24 °C; Table 1).

cSTIM– $L_{\text{full}}$  in high  $\text{Ca}^{2+}$  showed the highest thermal stability of any ortholog examined (Table 1). To examine whether this enhanced stability was related to a change in  $\text{Ca}^{2+}$  binding affinity, we performed a direct radioactive  $^{45}\text{Ca}^{2+}$  binding assay. The apparent equilibrium dissociation constant ( $K_d$ ) fitted by the Hill equation was  $0.40 \pm 0.02$  mM (Fig. 5). The  $\text{Ca}^{2+}$  binding profile showed a high apparent cooperativity with a Hill coefficient of  $3.15 \pm 0.31$ . Furthermore, the curve showed

---

directed away from the cleft in *C. elegans* in contrast to human STIM2 EF–SAM are labeled and shown as orange sticks. (D) Hydrophobic residue packing into the EF-hand cleft of *C. elegans* STIM. The hydrophobic anchor residues (red sticks) of the SAM– $\alpha$ 10 helix is shown relative to the EF-hand cleft residues (yellow sticks). (E) EF-hand:SAM domain– $\alpha$ 10 ionic interaction of *C. elegans* STIM. The basic R85 (blue sticks) is shown relative to the D177 (red sticks) of the SAM– $\alpha$ 10 helix. Interatomic distances are shown with black dashed lines. (F) Electrostatic surface potential of the cSTIM– $L_{\text{full}}$ . The gradient shown is from –3 (acidic, red) to +3 (basic, blue) kT/e. Locations of acidic (red font) and basic residues (blue font) are indicated. In (A) and (D), the  $\text{Ca}^{2+}$  ion is shown as a yellow sphere. In (A) and (C)–(F), the amino (N) and carboxyl (C) termini are labeled.

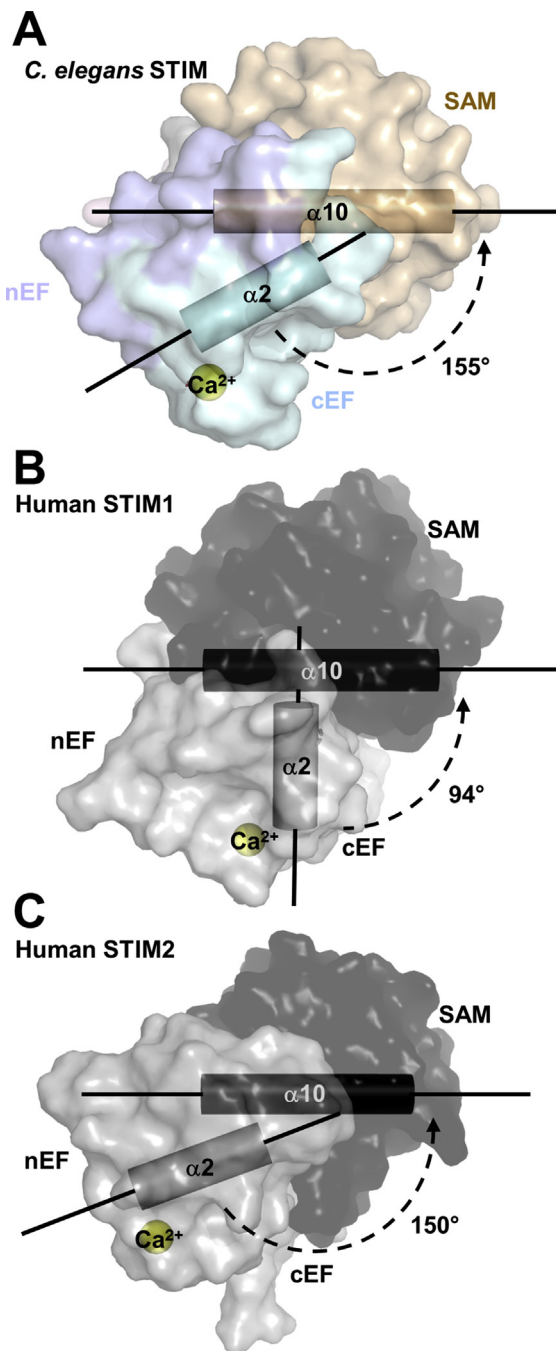


**Fig. 2.** EF-hand relative to SAM domain orientation for human and *Caenorhabditis elegans* STIMs. The interhelical angles of the  $\alpha_2$  helix (canonical EF-hand) relative to the  $\alpha_{10}$  helix (SAM domain) of (A) *C. elegans* STIM, (B) human STIM1, and (C) human STIM2 are shown. The long axes (black solid lines) of the  $\alpha_2$  and  $\alpha_{10}$  helices (cylinders) used for the interhelical angle calculations are shown. In (B) and (C), the SAM domain (black surface) relative to the EF-hand domain (gray surface) is shown, and the STIM1 and STIM2 EF–SAM PDB codes used were 2K60 and 2L5Y, respectively. In (A)–(C), the  $\text{Ca}^{2+}$  ion is shown as a yellow sphere.

saturation at a  $\text{Ca}^{2+}$ :protein molar ratio of  $1.05 \pm 0.02$ , indicating a single  $\text{Ca}^{2+}$  binding site, consistent with our crystal data (Fig. 5). The apparent positive cooperativity may be due to a coupling between  $\text{Ca}^{2+}$  binding and protein folding, a highly cooperative process for globular proteins. The fitted  $K_d$  for the *C. elegans* STIM luminal domain suggests a sub-mM affinity, similar to the ~0.2–0.6 mM and ~0.5–0.8 mM affinities measured for human STIM1 and STIM2 EF–SAM proteins, respectively [26,29]. Thus, the structural features adopted by the *C. elegans* luminal domain in the  $\text{Ca}^{2+}$  bound state play a dominant role in conferring the highest stability of any of the STIM proteins studied to date.

#### The *C. elegans* STIM luminal domain shows folded and unfolded conformations in low $\text{Ca}^{2+}$

Having established that human STIM1, human STIM2, and *C. elegans* luminal STIM proteins that are extended to include the respective variable N-terminal domains have enhanced stability compared with the EF–SAM core proteins alone in low  $\text{Ca}^{2+}$ , we acquired solution  $^1\text{H}$ – $^{15}\text{N}$ -heteronuclear single quantum coherence (HSQC) spectra of each of the extended proteins to reveal structural details of the conformations. In the presence of excess  $\text{Ca}^{2+}$ , all proteins showed a well-dispersed  $^1\text{H}$ – $^{15}\text{N}$ -HSQC spectrum with the expected number of amide H(N) crosspeaks and relatively homogeneous intensities (Fig. S4A–C). In low  $\text{Ca}^{2+}$ , STIM1–N<sub>ext</sub> showed severe peak broadening and a collapse of all visible H(N) peaks into the central ~7.5–8.5 ppm  $^1\text{H}$  region of the spectrum, even at relatively low protein concentration (i.e., ~50  $\mu\text{M}$ ) and temperature (i.e., 10 °C) (Fig. S4A). On the other hand, the H(N) crosspeaks of STIM2–N<sub>ext</sub> and cSTIM–L<sub>full</sub> remained better dispersed in the  $^1\text{H}$ – $^{15}\text{N}$ -HSQC spectra acquired under similar low  $\text{Ca}^{2+}$  conditions (Fig. S4B and C). Although the spectra from both the STIM2 and *C. elegans* proteins clearly showed an increase in the number of peaks collapsed into the central ~7.5–8.5 ppm  $^1\text{H}$  region, the H(N) peak intensities were more homogeneous for *C. elegans* (Fig. S4B and C). Thus, we pursued backbone atom chemical shift assignments of cSTIM–L<sub>full</sub>, as this construct was taken to be the most tractable for atomic resolution structural analyses in low  $\text{Ca}^{2+}$ .

We completed ~95 and ~75% of the backbone atom chemical shift assignments of cSTIM–L<sub>full</sub> in high and low  $\text{Ca}^{2+}$ , respectively. The chemical shift index (CSI) shows that in solution and high  $\text{Ca}^{2+}$ , cSTIM–L<sub>full</sub> adopts secondary structure elements very similar to the crystal state (Fig. S5A). Remarkably, in low  $\text{Ca}^{2+}$ , the protein showed two structural forms, as indicated by two distinct tracts of connectivity in the three-dimensional (3D) spectra acquired for the sequential backbone atom assignments and corresponding peak doubling in the

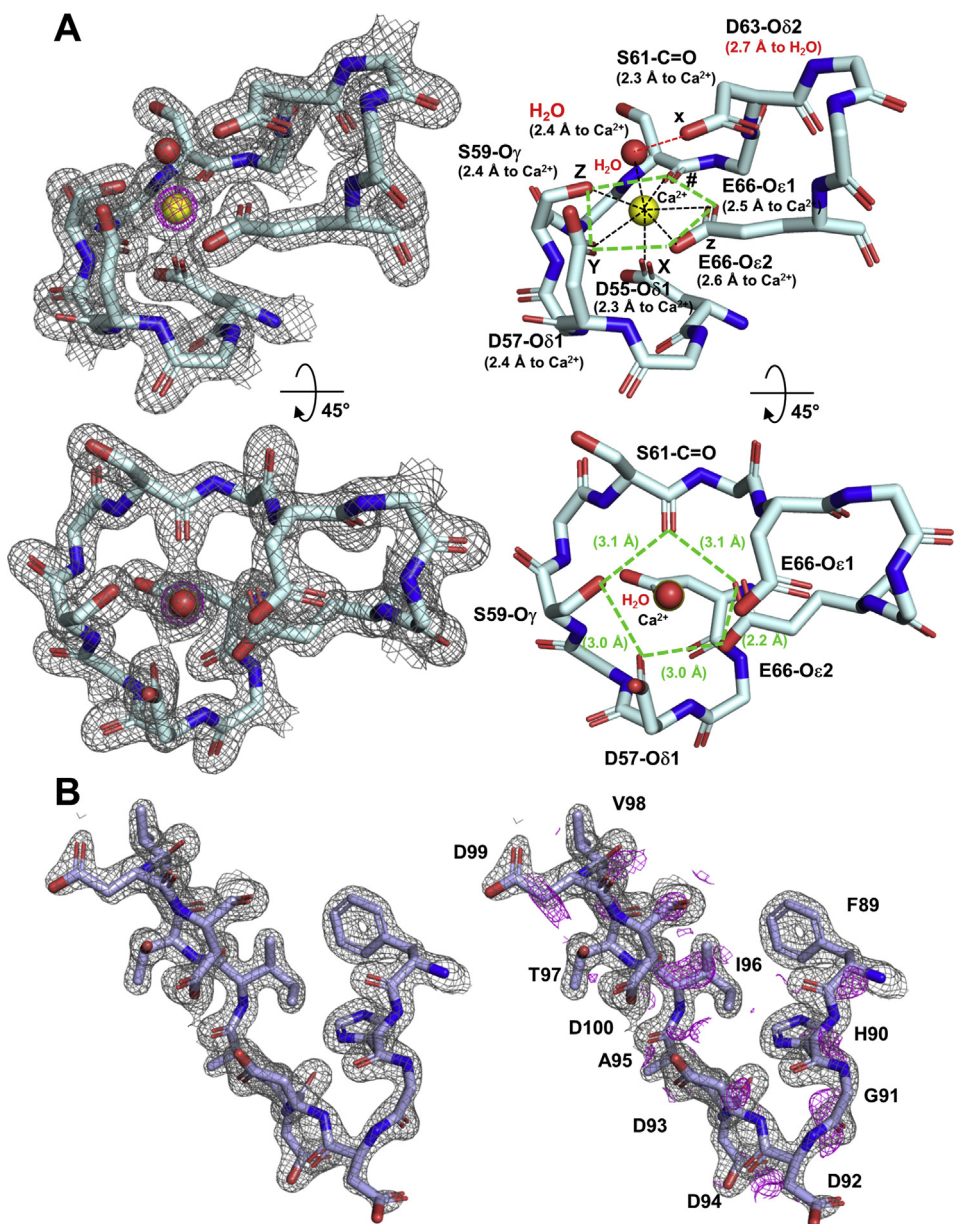


**Fig. 3.**  $\text{Ca}^{2+}$  ion coordination geometry in the *Caenorhabditis elegans* EF-hand loops. (A) The  $2\text{F}_0 - \text{F}_c$  electron density map contoured at  $2.0\sigma$  (gray mesh) relative to the polypeptide chain model of the canonical EF-hand loop (sticks),  $\text{Ca}^{2+}$  ion (yellow sphere), and water molecule (red sphere) is shown at left. At left, the  $\text{F}_0 - \text{F}_c$  ( $9.0\sigma$ ) omit map (magenta mesh) shows unaccounted-for density in the absence of the  $\text{Ca}^{2+}$  ion. The pentagonal (green dashed lines) bipyramidal coordination geometry of the  $\text{Ca}^{2+}$  ion by seven oxygen atoms is shown at right. The distances of each of the liganding oxygen atoms to the  $\text{Ca}^{2+}$  ion (dashed black lines) are indicated below the atom name. The distance (red dashed line) to the water molecule (red sphere) is indicated below the oxygen atom name in red font. The X, Y, Z, #, x, and z residues corresponding to the loop positions shown in Fig. 1C are labeled adjacent to the side chain. (B) The  $2\text{F}_0 - \text{F}_c$  electron density map contoured at  $2.0\sigma$  (gray mesh) relative to the polypeptide chain model of the noncanonical EF-hand loop (sticks) is shown at left. At right, the  $\text{F}_0 - \text{F}_c$  ( $2.0\sigma$ ) omit map shows no unaccounted-for density (magenta mesh) in the space encompassed by the loop, indicating no ion coordination in the noncanonical EF-hand loop.

$^1\text{H}-^{15}\text{N}$ -HSQC spectrum (Fig. 6A). The CSI for each of these conformations show that the  $\alpha 0$  and  $\alpha 1$  of one state remains structured (form 1), whereas these helices become more unstructured in a second state (form 2) (Fig. S5B). Most unassigned

residues in form 1 and form 2 cluster on the canonical EF-hand loop,  $\alpha 2$ ,  $\alpha 3$  and the noncanonical EF-hand loop. The difficulty in assigning the chemical shifts for residues in this EF-hand region in low  $\text{Ca}^{2+}$  is due to poor chemical shift dispersion

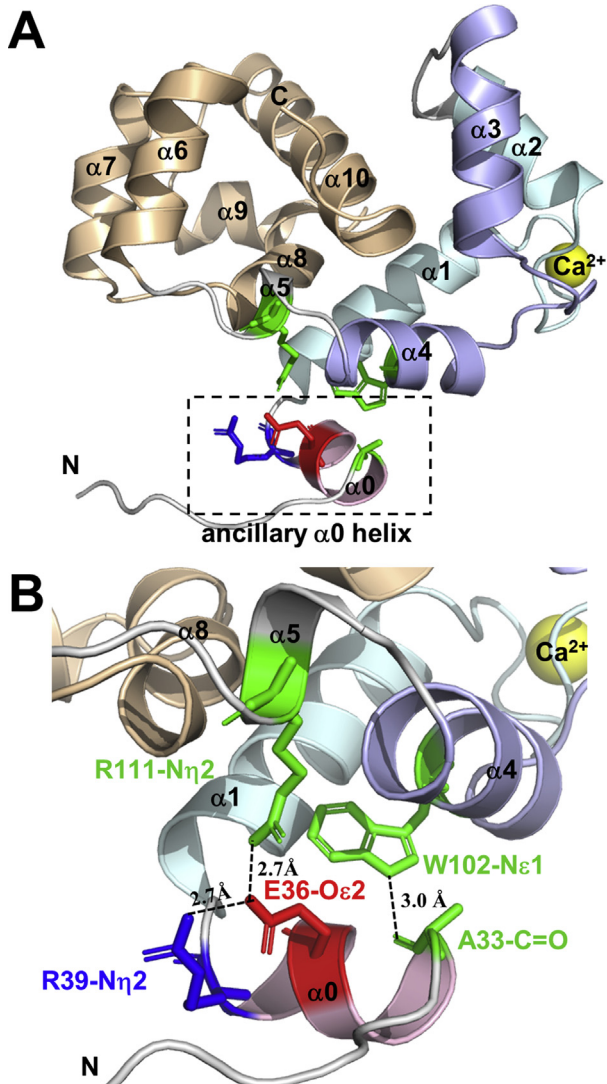


**Fig. 4.** Ancillary  $\alpha_0$  helix in the nonconserved N-terminal region of *Caenorhabditis elegans* STIM. (A) Location of  $\alpha_0$  (pink cartoon; dashed black box) relative to the EF-SAM domain. (B) Zoomed view of the contacts made between  $\alpha_0$ ,  $\alpha_1$ , and  $\alpha_4$ . The  $\alpha_0$  intrahelix ionic interaction between R39 (blue sticks) and E36 (red sticks), interhelix ionic interaction between  $\alpha_0$ -E36 and  $\alpha_5$ -R111 (green sticks), and interhelix H-bond between  $\alpha_0$ -A33 (green sticks) and  $\alpha_4$ -W102 (green sticks) are shown. The distances between the atoms involved in these contacts are indicated with dashed black lines. In (A) and (B), the  $\text{Ca}^{2+}$  ion is shown as a yellow sphere.

caused by protein unfolding and possibly conformational exchange of residues involved in dimerization/oligomerization. The SAM domain remains largely structured and  $\alpha$ -helical for both forms detected in low  $\text{Ca}^{2+}$  (Fig. S5B).

Interestingly, the CSI of the C-terminal region of the forms 1 and 2 show a propensity for formation of a short  $\beta$ -strand between ~residues 177–185

(Fig. S5B). In the  $\text{Ca}^{2+}$ -bound state, this region of cSTIM–L<sub>full</sub> folds into part of the long  $\alpha_{10}$  helix. Thus,  $\alpha_{10}$  undergoes a structural transition from  $\alpha$ -helix to  $\beta$ -strand upon  $\text{Ca}^{2+}$  depletion (Fig. S5A and B). Indeed, some of the largest magnitude  $^1\text{H}(^{15}\text{N})$  chemical shift perturbations (CSP) occur at this C-terminal region when comparing the conformations in high and low  $\text{Ca}^{2+}$  (Fig. 6B). Additional large CSPs are observed in the  $\alpha_0$  and  $\alpha_1$  helices, which become more unstructured in low  $\text{Ca}^{2+}$  (Fig. 6B).

To assess the structural integrity of the  $\beta$ -strand, which was detected in both low  $\text{Ca}^{2+}$  forms of cSTIM–L<sub>full</sub>, we used NMR to probe the solution dynamics of the protein. We focused on form 1 because the relative abundance was higher based on peak intensities in the HSQC (Fig. S6). In high  $\text{Ca}^{2+}$ , the  $^{15}\text{N}-\{^1\text{H}\}$ -heteronuclear NOEs indicated a stably formed structure with low backbone flexibility on the ~ns timescale. Specifically, the data showed that most residues show saturated/reference peak intensity ratios of >0.8, excluding residues near the N- and C-termini, which show markedly decreased ratios between residues ~23–30 and ~184–192, respectively (Fig. S6). In low  $\text{Ca}^{2+}$ , these terminal residues similarly show a high degree of flexibility on the ~ns timescale; however, the residues in between the unassigned canonical EF-hand loop,  $\alpha_2$ ,  $\alpha_3$ , and the noncanonical EF-hand loop show enhanced mobility compared with the state observed in high  $\text{Ca}^{2+}$  (Fig. S6). Further, although the mobility of the residues involved in  $\beta$ -strand formation appears unaffected by the loss of  $\text{Ca}^{2+}$ , the six residues immediately upstream (i.e., residues ~172–178) of the  $\beta$ -strand show an increased mobility on the ~ns timescale (Fig. S6). Thus, the  $\beta$ -strand formation may be facilitated and/or promoted by an unstructuring or increased mobility of residues immediately upstream of the far C-terminal motif.

#### The far C-terminal region of the *C. elegans* STIM luminal domain affects folding, stability, and oligomerization kinetics

Having discovered a propensity for the C-terminal residues of  $\alpha_{10}$  to undergo an  $\alpha$ -helix (in high  $\text{Ca}^{2+}$ ) to  $\beta$ -strand (in low  $\text{Ca}^{2+}$ ) transition, we then assessed the role of the transitioning residues in the folding and stability of cSTIM–L<sub>full</sub> with and without  $\text{Ca}^{2+}$ . Our crystal structure revealed that L180 is an important anchor residue that packs into the EF-hand cleft in high  $\text{Ca}^{2+}$ ; moreover, our solution NMR data showed the L180 undergoes an  $\alpha$ -helix to  $\beta$ -strand transition in low  $\text{Ca}^{2+}$ . Thus, within the hydrophobic V178–V179–L180–F181 stretch at the C-terminus, we created two separate double mutations to probe how residue variability in this region affects the structure and stability of the entire luminal domain: (i) V178A–V179A–L180–F181 (AALF mutant) and (ii)

**Table 1.** Thermal stability of STIM luminal domain constructs.

Name <sup>a</sup>	Species	Residue range <sup>b</sup>	Paralog	+ $\text{Ca}^{2+}$	- $\text{Ca}^{2+}$	$\Delta T_m$ , $\text{Ca}^{2+}$ (°C)	$\Delta T_m$ , mut (°C)
				$T_m$ <sup>c</sup> (°C)	$T_m$ <sup>d</sup> (°C)		
hSTIM1-EF-SAM <sup>g</sup>	<i>Homo sapiens</i>	58–201	STIM1	45.0	21.0	24.0	
hSTIM2-EF-SAM <sup>h</sup>	<i>H. sapiens</i>	62–205	STIM2	50.0	36.0	14.0	
hSTIM1-N <sub>ext</sub>	<i>H. sapiens</i>	40–201	STIM1	60.5	36.5	24.0	
hSTIM2-N <sub>ext</sub>	<i>H. sapiens</i>	44–205	STIM2	61.5	50.0	11.5	
cSTIM-L <sub>full</sub>	<i>Caenorhabditis elegans</i>	23–192	STIM	63.5	49.5	14.0	
cSTIM-L <sub>ΔN</sub>	<i>C. elegans</i>	40–192	STIM	56.0	37.0	19.0	
cSTIM-L <sub>full</sub> (VVAA)	<i>C. elegans</i>	23–192	STIM	44.0	36.0	8.0	13.5
cSTIM-L <sub>full</sub> (AALF)	<i>C. elegans</i>	23–192	STIM	48.0	12.5	35.5	37.0

<sup>a</sup> N<sub>ext</sub> denotes N-terminally extended relative to EF-SAM; L<sub>full</sub> denotes full luminal domain; L<sub>ΔN</sub> denotes N-terminal deletion relative to the full luminal domain.

<sup>b</sup> *H. sapiens* STIM1, *H. sapiens* STIM2, *C. elegans* STIM residue ranges are from NCBI accession numbers AFZ76986.1, Q9P246.2, and ABG89384.1, respectively.

<sup>c</sup>  $T_m$  was taken as the temperature where the fractional change in CD signal was 0.5 in the presence of 5 mM  $\text{CaCl}_2$ .

<sup>d</sup>  $T_m$  was taken as the temperature where the fractional change in CD signal was 0.5 in the absence of  $\text{CaCl}_2$ .

<sup>e</sup>  $\Delta T_m$ ,  $\text{Ca}^{2+}$  was taken as  $T_m$  (+ $\text{Ca}^{2+}$ ) –  $T_m$  (- $\text{Ca}^{2+}$ ).

<sup>f</sup>  $\Delta T_m$ , mut was taken as  $T_m$  [cSTIM-L<sub>full</sub>(wild-type, - $\text{Ca}^{2+}$ )] –  $T_m$  [cSTIM-L<sub>full</sub>(mutant, - $\text{Ca}^{2+}$ )].

<sup>g</sup> Taken from Refs. [26,27].

<sup>h</sup> Taken from Refs. [28,29].

V178–V179–L180A–F181A (VVAA mutant). Far-UV CD spectra were acquired in high and low  $\text{Ca}^{2+}$  to assess secondary structure. In the presence of excess  $\text{Ca}^{2+}$  and at 4 °C, the AALF and VVAA proteins showed a high level of  $\alpha$ -helicity, as indicated by the strong negative ellipticity observed at ~208 and 222 nm. In low  $\text{Ca}^{2+}$ , both the AALF and VVAA double mutant proteins showed a marked loss in negative ellipticity at ~208 and 222 nm, indicative of decreased  $\alpha$ -helicity (Fig. 7A and B). However, the loss in negative ellipticity for these mutants was greater than observed for the wild-type cSTIM-L<sub>full</sub> protein, and the spectra showed a shift to lower

wavelength for the ~208 nm minimum. These spectral differences imply that the VVAA and AALF mutations result in a less well-folded states in low  $\text{Ca}^{2+}$  compared with wild-type cSTIM-L<sub>full</sub> (Fig. S3A).

The thermal stability was also assessed by monitoring changes in CD ellipticity at 225 nm. In the presence of excess  $\text{Ca}^{2+}$  (i.e., 5 mM  $\text{CaCl}_2$ ), the  $T_m$  of the AALF and VVAA double mutant proteins was decreased by ~15.5 and 19.5 °C, respectively, compared with wild-type (Table 1), consistent with the role of this C-terminal  $\alpha$ 10 region in packing into the EF-hand hydrophobic cleft. In low  $\text{Ca}^{2+}$ , the VVAA mutant showed a  $T_m$  drop of ~13.5 °C, and the AALF double mutant  $T_m$  decreased an astonishing ~37.0 °C (Fig. 7C and D).

Then, we performed size-exclusion chromatography with in-line multiangle light scattering (SEC-MALS) to assess the quaternary structure of cSTIM1-L<sub>full</sub> at stabilizing temperatures (i.e., 4 °C). In high  $\text{Ca}^{2+}$ , wild-type, VVAA and AALF versions of cSTIM-L<sub>full</sub> all eluted similarly as monomers (Fig. 7E). In low  $\text{Ca}^{2+}$ , all proteins showed a shift to earlier elution volumes, indicating a change in particle size and/or shape. The wild-type and VVAA protein remained primarily monomeric despite the apparent conformational change. In contrast, cSTIM-L<sub>full</sub>-AALF formed dimers and larger oligomers in low  $\text{Ca}^{2+}$ , readily detectable even at low concentration and temperature, consistent with the extreme destabilization observed for this mutant (Fig. 7E). Finally, we assessed the self-association kinetics of wild-type, VVAA and AALF using static light scattering at a higher temperature (i.e., 37 °C). As expected given the rank order of thermal stabilities, the AALF protein showed the fastest, and the wild-type protein showed the slowest self-association kinetics (Fig. 7F).

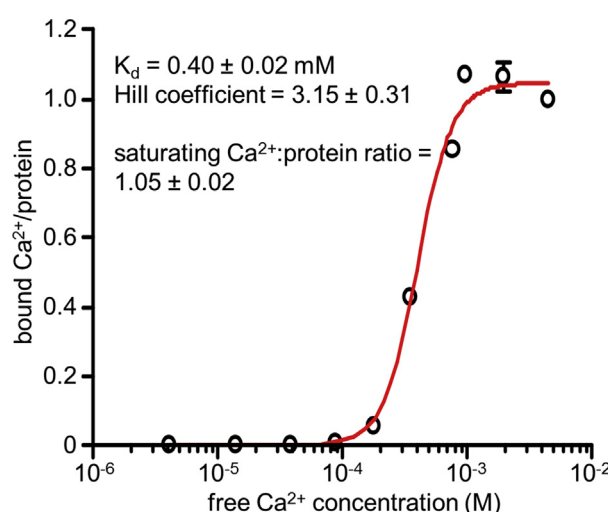


**Fig. 5.** Direct  $^{45}\text{Ca}^{2+}$  binding to cSTIM-L<sub>full</sub>.  $\text{Ca}^{2+}$  binding data were acquired at ambient temperature for 0.1 mM protein in 20 mM Tris, 100 mM NaCl, pH 7.5, and fit to the Hill equation. Mean  $\pm$  SD from three independent measurements.

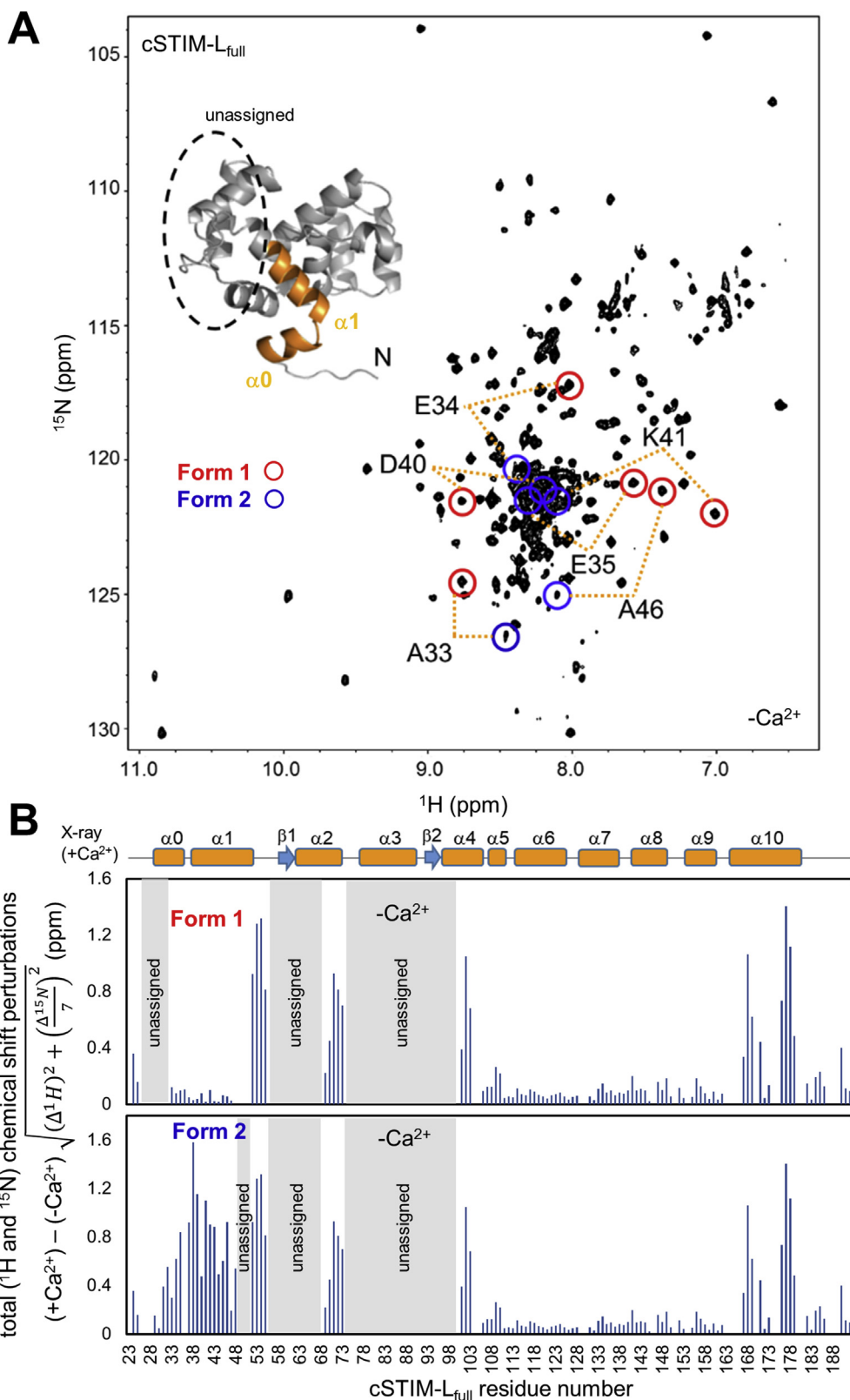


**Fig. 6.** Solution NMR characterization of cSTIM-L<sub>full</sub>. (A)  $^1\text{H}$ - $^{15}\text{N}$ -HSQC spectrum of cSTIM-L<sub>full</sub> in low  $\text{Ca}^{2+}$ . Representative  $^1\text{H}$ ( $^{15}\text{N}$ ) crosspeaks showing peak doubling based on connectivities observed in 3D backbone NMR experiments are circled. The dashed black ellipse indicates the region of the EF-SAM structure that remains unassigned.

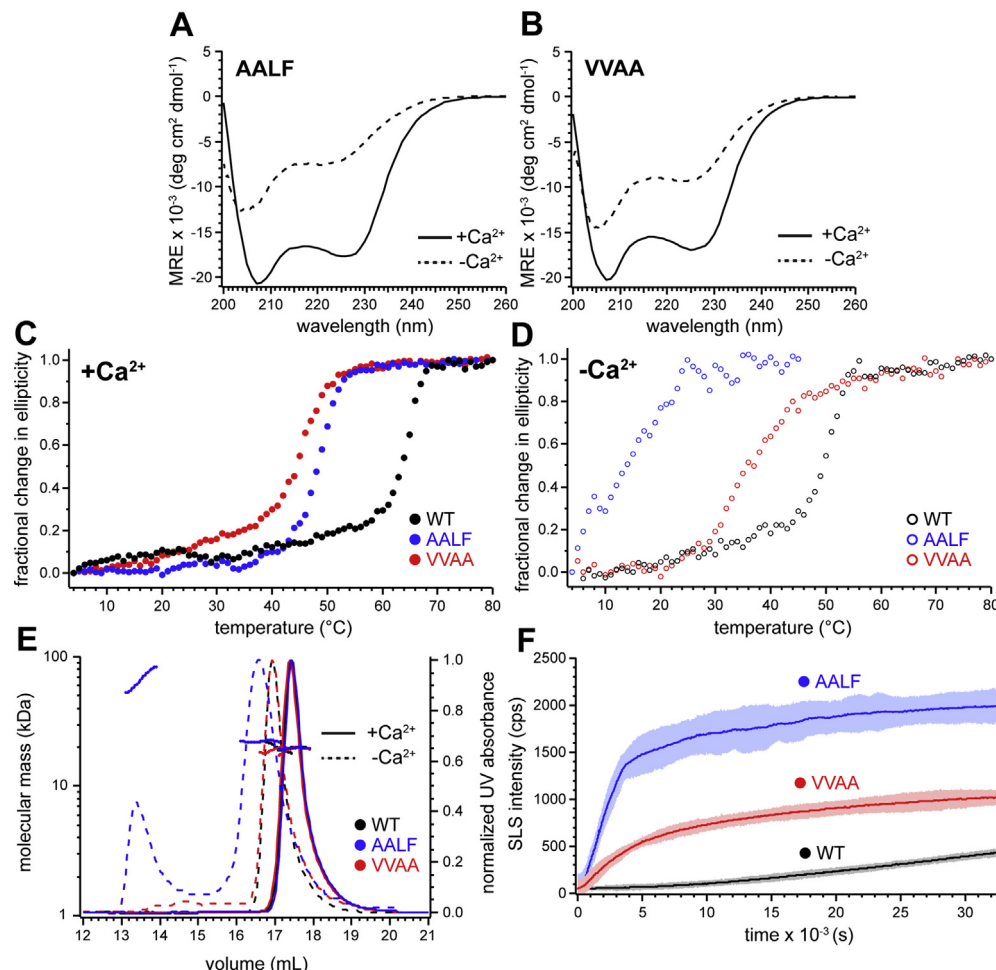


**Fig. 7.** Biophysical characteristics of cSTIM–L<sub>full</sub>. Far-UV CD spectra of cSTIM–L<sub>full</sub>–AALF (A) and cSTIM–L<sub>full</sub>–VVAA (B) in the presence (solid lines) and absence (dashed lines) of 5 mM  $\text{Ca}^{2+}$ . (C) Thermal denaturation profiles of wild-type cSTIM–L<sub>full</sub> (black-filled circles), cSTIM–L<sub>full</sub>–AALF (blue-filled circles), cSTIM–L<sub>full</sub>–VVAA (red-filled circles) protein in the presence of 5 mM  $\text{Ca}^{2+}$ . (D) Thermal denaturation profiles acquired by monitoring changes in CD signal at 225 nm as a function temperature for wild-type cSTIM–L<sub>full</sub> (black open circles), cSTIM–L<sub>full</sub>–AALF (blue open circles), cSTIM–L<sub>full</sub>–VVAA (red open circles) protein in the absence of  $\text{Ca}^{2+}$ . (E) SEC-MALS of wild-type cSTIM–L<sub>full</sub> (black), cSTIM–L<sub>full</sub>–AALF (blue), and cSTIM–L<sub>full</sub>–VVAA (red) in the absence (dashed lines) and presence of 5 mM  $\text{Ca}^{2+}$  (solid lines). Molecular weights shown were calculated over the major peaks of interest (filled circles). (F) Kinetics of self-association for wild-type cSTIM–L<sub>full</sub> (black lines), cSTIM–L<sub>full</sub>–VVAA (red lines), and cSTIM–L<sub>full</sub>–AALF (blue lines) in low  $\text{Ca}^{2+}$ . The change in SLS intensity as a function of time was measured at 37 °C. Mean  $\pm$  SD (shadow) from three independent measurements. Data in (A), (B), and (E) were acquired at 4 °C. Data in (A)–(F) were acquired in 20 mM Tris, 100 mM NaCl, pH 7.5. Wild-type cSTIM–L<sub>full</sub> data in (C) and (D) are reproduced from Fig. S3.

Collectively, these biophysical data indicate that the inherent amino acid composition of the far C-terminal region of cSTIM–L<sub>full</sub> can radically modulate the structure, stability, and self-association of the domain, which has important implications for triggering STIM and SOCE activation.

## Discussion

The solution NMR structures of human STIM1 and STIM2 EF–SAM have been determined in high  $\text{Ca}^{2+}$  [27,29]. There is a high structural conservation between human STIM1 and STIM2 EF–SAM, as

The  $\alpha$ 0 and  $\alpha$ 1 helix regions that show two discernible states (form 1 and form 2) are colored orange. (B) Total  $^1\text{H}$  and  $^{15}\text{N}$  chemical shift perturbations observed in  $^1\text{H}$ – $^{15}\text{N}$ -HSQC spectra of cSTIM–L<sub>full</sub> acquired in high and low  $\text{Ca}^{2+}$  solution conditions. The secondary structure components elucidated in the  $\text{Ca}^{2+}$ -bound crystal structure are indicated above the corresponding residue range. In (A) and (B), data were acquired at 0.15 mM protein in 20 mM Tris, 100 mM NaCl, pH 7.5 at 15 °C with or without high  $\text{Ca}^{2+}$  as indicated.

both show a hydrophobic cleft formed by the EF-hand domain and the packing of a five-helix bundle SAM domain into the cleft, which is primarily mediated by the  $\alpha 10$  helix. The intramolecular EF-hand:SAM– $\alpha 10$  interaction occurs akin to the manner that calmodulin recognizes myriad target peptides with hydrophobic anchor residues penetrating into the nonpolar pocket [27,44,52]. The sequence identity between human STIM1 and STIM2 EF–SAM domains is ~58% [53]. In comparison, the sequence identities between the *C. elegans* EF–SAM core and the human paralogs are 40% and 38% for STIM1 and STIM2, respectively [53]. Here, our crystal structure clearly reveals a high structural conservation between *C. elegans* EF–SAM and the human STIM1 and STIM2 solution structures, consistent with the high sequence conservation of EF–SAM from mammals to roundworms and indicative of a common  $\text{Ca}^{2+}$  sensing mechanism among STIM phylogeny. In *C. elegans*, EF–SAM the L176 and L180 of  $\alpha 10$  represent the anchor residues that pack into the EF-hand cleft. The EF-hand:SAM domain interaction in *C. elegans* is also buttressed by an ionic interaction between the  $\alpha 3$  R85 residue and the D177 on  $\alpha 10$ . Human STIM2 EF–SAM, but not STIM1, shows a similar EF-hand:SAM domain ionic interaction between K108 of  $\alpha 3$  and D200 of  $\alpha 10$  [29]. K108 and D200 of human STIM2 align with R85 and D177 of *C. elegans* STIM. Given the similar locations of ionic and hydrophobic interactions in human STIM2 and *C. elegans* STIM EF–SAM domains, it is not unexpected that these two proteins share very similar EF-hand:SAM domain orientations (Fig. 2).

Our work also reveals that the nonconserved luminal region, upstream of EF–SAM plays a direct role in stabilizing the EF–SAM fold. Our crystal structure of cSTIM–L<sub>full</sub> showed that an ancillary helix ( $\alpha 0$ ) forms in this nonconserved region; further,  $\alpha 0$  interacts with both the EF-hand and  $\alpha 5$  helix linker, acting as a brace that holds the immediately adjacent  $\alpha 1$ ,  $\alpha 4$ , and  $\alpha 5$  in place (Fig. 4). Despite sequence divergence between human STIM1, STIM2, and *C. elegans* STIM in this region upstream of EF–SAM [53], our solution experiments showed that each of these luminal domains devoid of this nonconserved segment is less thermally stable in both  $\text{Ca}^{2+}$ -bound and  $\text{Ca}^{2+}$ -free states (Table 1). Thus, it is tempting to speculate that the interaction of the nonconserved N-terminal region with the EF–SAM core protein is a conserved structural mechanism capable of stabilizing all STIM molecules. Indeed, it was recently shown that this nonconserved region of human STIM1 contacts W121 and K122 of the  $\alpha 4$  helix of EF–SAM [42]. Remarkably, W121 of human STIM1 aligns with W102 of *C. elegans* STIM, an important contact residue for  $\alpha 0$  elucidated in our crystal structure. Further, S-nitrosylation of Cys residues within this

nonconserved region of STIM1 was found to further thermodynamically stabilize the full luminal domain of the protein, concomitant with an inhibition of STIM1 activation and SOCE [42,49]. In contrast, S-glutathionylation of these Cys residues (i.e., C56) weakened  $\text{Ca}^{2+}$  binding affinity of the human STIM1 luminal domain, resulting in constitutive SOCE [50]. Therefore, sequence variability in the region upstream of EF–SAM may have evolved commensurate with an ability to undergo luminal-specific posttranslational modifications that can modulate EF–SAM stability and STIM function depending on specific environmental cues.

Interestingly, our solution NMR data reveal that two different conformations are sampled by cSTIM–L<sub>full</sub> in low  $\text{Ca}^{2+}$ . The SAM domain remains well folded, whereas the  $\beta 1$ ,  $\alpha 2$ ,  $\alpha 3$ ,  $\beta 2$ , and a portion of  $\alpha 4$  of the EF-hand domain is likely unfolded in both states. In contrast,  $\alpha 0$  and  $\alpha 1$  are well folded in form 1 and become unfolded in form 2 (Fig. 6 and Fig. S5). The two conformations provide a possible mechanistic explanation for the enhanced stability observed for the S-nitrosylated human STIM1 luminal domain in low  $\text{Ca}^{2+}$ . Because  $\alpha 0$ ,  $\alpha 1$ , a portion of  $\alpha 4$  and  $\alpha 5$  remain folded in form 1, stabilizing  $\alpha 0$  contacts with  $\alpha 4$  and  $\alpha 5$  may be maintained in low  $\text{Ca}^{2+}$ . In the case of human STIM1, the S-nitrosylation in the nonconserved region may favor these contacts compared with the unmodified state. Nevertheless, high-resolution structural information is needed to tease out the precise stabilization mechanisms of the full human STIM1 luminal domains.

Remarkably, we also found that both forms of cSTIM–L<sub>full</sub> detected in low  $\text{Ca}^{2+}$  show an  $\alpha$ -helix to  $\beta$ -strand transition near the end of the  $\alpha 10$  helix. Given that  $\beta$ -strands are not stable in the absence of H-bonding, we speculated that  $\beta$ -strands from two STIM luminal domains may pair as the mechanism driving EF–SAM dimerization in low  $\text{Ca}^{2+}$ . Thus, we created VVAA and AALF mutations in  $\alpha 10$ , which decrease the predicted  $\beta$ -strand propensity based on PSIPRED analysis [54]. However, we found that these mutations markedly destabilize the cSTIM–L<sub>full</sub> proteins in high and low  $\text{Ca}^{2+}$ , and rather than suppressing potential  $\beta$ -sheet-mediated dimerization, increase the self-association kinetics (Fig. 7). Thus,  $\beta$ -sheet formation in this  $\alpha 10$  region could be more involved in stabilizing the higher order quaternary structure after dimerization/oligomerization occurs, and dimerization is likely primarily driven by the unfolding events revealed in the EF-hand domain by our NMR work (see above).

Recent work using a chimera of human EF–SAM fused to *Thermus thermophilus* GroP-like gene E (GrpE), which restricts EF–SAM movement within strictly forming GrpE dimers, proposed that human EF–SAM binds up to ~5–6  $\text{Ca}^{2+}$  ions, not only to the canonical EF-hand site but also to multiple unconventional surface sites [55]. Here, our work

provides the first direct atomic resolution insights into  $\text{Ca}^{2+}$  binding, elucidating a single  $\text{Ca}^{2+}$  binding site within each *C. elegans* EF–SAM protomer, even in the context of dimers making up the asymmetric unit and 10 mM  $\text{CaCl}_2$  (Fig. 2 and Fig. S3). No additional  $\text{Ca}^{2+}$  binding sites were observed in this study. Further, we show that the  $\text{Ca}^{2+}$  ion is coordinated with pentagonal bipyramidal geometry in the EF-hand loop, as observed with classical EF-hand proteins such as calmodulin. In addition, no areas of unaccounted-for electron density were observed in our  $F_o - F_c$  omit maps other than the canonical  $\text{Ca}^{2+}$  binding site, when the single  $\text{Ca}^{2+}$  ion was removed. Nevertheless, we cannot exclude the possibility of more  $\text{Ca}^{2+}$  ions transiently interacting with the highly electrostatically negative surface of the luminal domain and that transient  $\text{Ca}^{2+}$  binding events may play a role promoting the canonical  $\text{Ca}^{2+}$  binding revealed by our crystal structure. Interestingly, the work by Gudlur et al. also showed that large-scale unfolding does not occur within either the EF-hand or SAM domains in low  $\text{Ca}^{2+}$  [55]. Consistently, our solution NMR data of *C. elegans* EF–SAM in low  $\text{Ca}^{2+}$  shows that the SAM domain remains largely folded. In contrast, we find that regions of the EF-hand domain unequivocally become conformationally unstable, adopting unfolded states. Ultimately, high-resolution characterization of the structural dynamics of the STIM luminal domain in low  $\text{Ca}^{2+}$  remains an important milestone for fully understanding STIM activation.

Interestingly, knockdown of the ER  $\text{Ca}^{2+}$  pump causes the unfolded protein response in *C. elegans*, yet a similar response is not induced by STIM knockdown in these roundworms, consistent with the protein unfolding events revealed by our work [56]. In *C. elegans*, STIM knockdown causes sterility due to the importance of SOCE in the function of sheath cells and spermatheca required for ovulation [56,57]. Transgenic worms expressing constitutively active STIM show severe arrhythmia in the posterior body wall muscle contraction required for defecation [56]. When *C. elegans* STIM is expressed in HEK293 cells, the protein appears preclustered at ER–PM junctions; however, SOCE is not activated until ER  $\text{Ca}^{2+}$  stores are depleted [58]. A series of human STIM1–*C. elegans* STIM chimeras revealed that the cytosolic domain of *C. elegans* STIM mediates the preclustering of *C. elegans* STIM [58]. Thus, structural changes in EF–SAM caused by low  $\text{Ca}^{2+}$  is key to inducing the conformational rearrangement of the cytosolic domain necessary for STIM activation and subsequent Orai1 channel gating. Here, our work has shed light on these luminal structural changes that include stable single  $\text{Ca}^{2+}$  coordination in the canonical EF-hand loop at high  $\text{Ca}^{2+}$ , and conformational instability and unfolding of several motifs within the EF-hand domain as well as an  $\alpha$ -helix to  $\beta$ -strand transition in the SAM domain at low  $\text{Ca}^{2+}$ .

## Methods

### Protein constructs, expression, and purification

*C. elegans* STIM, human STIM1, and human STIM2 cDNAs were from Origene Technologies, Inc. All STIM luminal constructs were subcloned into pET28a vectors (Novagen, Inc.). The residue numbers of the STIM luminal domain constructs used in this study are described in Table 1. Recombinant expression and purification of all luminal domain STIM proteins containing an N-terminal hexahistidine ( $\text{His}_6$ ) tag were carried out as described previously [26,28,32]. All experiments except for crystallization were performed in 20 mM Tris–HCl (pH 7.5) containing 100 mM NaCl and 0.5 mM EDTA or 5 mM  $\text{CaCl}_2$  for low and high  $\text{Ca}^{2+}$  samples, respectively. In addition, STIM1– $N_{\text{ext}}$  and STIM2– $N_{\text{ext}}$  protein buffers were supplemented with 1 mM DTT. Protein concentrations were calculated using  $\epsilon_{280 \text{ nm}} = 1.182, 1.319, 1.342$ , and  $1.181 (\text{mg mL}^{-1})^{-1}$  for cSTIM– $L_{\text{full}}$ , cSTIM– $L_{\Delta N}$ , STIM1– $N_{\text{ext}}$ , and STIM2– $N_{\text{ext}}$ , respectively.

### Crystallization

For crystallization of cSTIM– $L_{\text{full}}$ , the L-selenomethionine-labeled protein was prepared in 20 mM Tris–HCl, 300 mM NaCl, and 10 mM  $\text{CaCl}_2$ . Crystals were grown at 4 °C in sitting and hanging drop plates (Hampton, HR3-114 and HR3-172) by mixing equal volumes of protein (10 mg  $\text{mL}^{-1}$ ) and crystallization buffer [18% (v/v) PEG 3,350, 8% (v/v) tacsimate, pH 5.6]. Crystals appeared in approximately a week. Crystals were cryoprotected by immersion in well solution supplemented with 25% (v/v) glycerol before flash freezing in liquid nitrogen.

### Data collection and crystal structure determination

Diffraction data were collected at the Canadian Light Source (CLS) beamline CMCF-BM (08B1-1). Data were processed with HKL-2000 (HKL Research Inc.). The initial phase and a model of the cSTIM– $L_{\text{full}}$  were calculated using MAD in AutoSol [59]. The structure was refined using PHENIX [60]. The model was completed with iterative cycles of model building in COOT [61] and refinement with PHENIX\_refine [60] and REFMAC [62]. The cSTIM– $L_{\text{full}}$  structure contains two molecules in the asymmetric unit. Crystallization data and refinement statistics are shown in Table S1.

### Far-UV circular dichroism spectroscopy

Far-UV CD spectra were recorded on a Jasco J-815 CD spectrometer (Jasco, Inc.). Data were collected using 0.1-cm path length ES quartz cuvettes. Wavelength scan rates were 20 nm  $\text{min}^{-1}$  with a response time of 8 s and bandwidth of 1 nm. Thermal melts were acquired in 1 °C

increments at a scan rate of  $1\text{ }^{\circ}\text{C min}^{-1}$ . All CD experiments were performed using  $0.4\text{ mg mL}^{-1}$  protein.

### Size exclusion chromatography with in-line multi-angle light scattering

SEC was performed on a Superdex 200 increase 10/300 GL column (GE Healthcare).  $100\text{ }\mu\text{L}$  of protein at  $2.0\text{ mg mL}^{-1}$  was injected onto the column for each experiment. Multiangle light scattering (MALS) measurements were performed in-line using the three-angle ( $45^\circ$ ,  $90^\circ$  and  $135^\circ$ ) miniDawn static light-scattering instrument with a 690-nm laser (Wyatt Technologies, Inc.). Molecular weight was calculated using ASTRA software (Wyatt Technologies, Inc.) based on Zimm plot analysis using a refractive index increment,  $d_n dc^{-1} = 0.185\text{ L g}^{-1}$ .

### Static light scattering

Self-association kinetics of cSTIM-L<sub>full</sub>-WT, -VVA, and -AALF was measured by using Unit (Unchained Labs). After 10 min of temperature equilibration, a final concentration of  $25\text{ mM}$  EDTA was added to the EF-SAM proteins ( $0.1\text{ mM}$ ) solubilized in  $5\text{ mM}$   $\text{CaCl}_2$  to induce self-association. SLS intensity was collected at  $266$  and  $473\text{ nm}$  every  $\sim 50\text{ s}$  for each time course.

### $^{45}\text{Ca}^{2+}$ binding assay

$^{45}\text{Ca}^{2+}$  radioisotope binding assays were performed as described previously [63]. Briefly, cSTIM-L<sub>full</sub> ( $0.1\text{ mM}$  protein), which was dissolved in  $0.45\text{ mL}$  of  $20\text{ mM}$  Tris,  $100\text{ mM}$  NaCl, pH 7.5, was placed in the sample compartment of an Amicon Ultra-0.5 mL concentrator ( $10\text{ kDa}$  molecular mass cutoff), and a  $1\text{ }\mu\text{Ci}$  bolus of  $^{45}\text{CaCl}_2$  solution was added to the protein solution. The sample was subjected to centrifugation (at  $5000\text{ rpm}$ ) in a table top centrifuge (Eppendorf, 5415D) at ambient temperature for  $30\text{ s}$ . Successive additions of nonradioactive  $\text{Ca}^{2+}$  were made to the protein solution, and the centrifugation procedure was repeated. The radioactivity in the filtrate (free  $\text{Ca}^{2+}$ ) and the radioactivity in an equal volume of the protein sample (total  $\text{Ca}^{2+}$ ) were determined by liquid scintillation counting.

### Solution NMR spectroscopy

Solution NMR data were acquired using a Bruker Avance 800 MHz spectrometers equipped with a cryogenic, triple-resonance probe (Bruker Biospin). Assignments of backbone atom chemical shifts were made using standard  $^1\text{H}-{}^{15}\text{N}$ -HSQC [64],  $^1\text{H}-{}^{15}\text{N}-{}^{13}\text{C}$ -HNCO [65],  $^1\text{H}-{}^{15}\text{N}-{}^{13}\text{C}$ -CBCA(CO)NH [66], and  $^1\text{H}-{}^{15}\text{N}-{}^{13}\text{C}$ -HNCACB [67] experiments. Spectra were processed using NMRPipe [68], and sequential assignments were made using NMRView [69]. Backbone relaxation data were acquired using an  ${}^{15}\text{N}-\{{}^1\text{H}\}$  heteronuclear pulse sequence [70] with and without a  $3\text{ s}$   ${}^1\text{H}$  saturation before  ${}^{15}\text{N}$  excitation. Secondary structure probability was determined from the assigned chemical shifts based on the chemical shift index [71]. The NMR buffer was  $20\text{ mM}$  Tris,  $100\text{ mM}$  NaCl, pH 7.5, and 7% (v/v) deuterium oxide ( $\text{D}_2\text{O}$ ).

### Accession numbers

The Protein Data Bank (PDB) accession number for the *C. elegans* STIM luminal domain (i.e., residues 23–192; cSTIM-L<sub>full</sub>) X-ray crystal structure determined in the presence of  $\text{Ca}^{2+}$  is 6PW7. The Biological Magnetic Resonance Data Bank accession numbers for the backbone atom chemical shifts of the *C. elegans* luminal domain (i.e., residues 23–192; cSTIM-L<sub>full</sub>) in the absence (form 1), absence (form 2), and presence of  $\text{Ca}^{2+}$  is 27981, 27982 and 27983, respectively.

### Acknowledgments

This work was supported by CIHR, HSFC, and NSERC operating grants to (M.I.) and an NSERC operating grant to (P.B.S.). We thank Masumi Kobayashi for her contributions to the initial stage of the project. We are grateful to CFI and Princess Margaret Cancer Foundation for support of the NMR facility and our research at Princess Margaret Cancer Centre (PM-CC)/UHN, Canada and to the CMCF beamline at the Canadian Light Source for assisting with data collection. M.I. holds a CRC in Cancer Structural Biology.

### Appendix A. Supplementary data

Supplementary data to this article can be found online at <https://doi.org/10.1016/j.jmb.2019.10.003>.

Received 28 July 2019;  
Received in revised form 17 September 2019;  
Accepted 7 October 2019  
Available online 15 October 2019

**Keywords:**  
Calcium binding stoichiometry;  
Stromal interaction molecule;  
EF-SAM;  
Crystal structure;  
*Caenorhabditis elegans*

\*Contributed equally to this work.

<sup>†</sup>Present Address: Jeol Resonance, Inc., Tokyo 196-8558, Japan.

<sup>‡</sup>Present Address: Black Diamond Therapeutics, Inc., Toronto, Canada M5G 0B7.

### References

- [1] J.W. Putney, Alternative forms of the store-operated calcium entry mediators, STIM1 and Orai1, *Curr. Top. Membr.* 71 (2013) 109–123.

- [2] M. Prakriya, R.S. Lewis, Store-operated calcium channels, *Physiol. Rev.* 95 (2015) 1383–1436.
- [3] R. Qiu, R.S. Lewis, Structural features of STIM and Orai underlying store-operated calcium entry, *Curr. Opin. Cell Biol.* 57 (2019) 90–98.
- [4] M.J. Berridge, M.D. Bootman, H.L. Roderick, Calcium signalling: dynamics, homeostasis and remodelling, *Nat. Rev. Mol. Cell Biol.* 4 (2003) 517–529.
- [5] S. Feske, E.Y. Skolnik, M. Prakriya, Ion channels and transporters in lymphocyte function and immunity, *Nat. Rev. Immunol.* 12 (2012) 532–547.
- [6] J. Roos, P.J. DiGregorio, A.V. Yeromin, K. Ohlsén, M. Lioudyno, S. Zhang, et al., STIM1, an essential and conserved component of store-operated  $\text{Ca}^{2+}$  channel function, *J. Cell Biol.* 169 (2005) 435–445.
- [7] S.L. Zhang, Y. Yu, J. Roos, J.A. Kozak, T.J. Deerinck, M.H. Ellisman, et al., STIM1 is a  $\text{Ca}^{2+}$  sensor that activates CRAC channels and migrates from the  $\text{Ca}^{2+}$  store to the plasma membrane, *Nature* 437 (2005) 902–905.
- [8] J. Liou, M.L. Kim, W.D. Heo, J.T. Jones, J.W. Myers, J.E. Ferrell Jr., et al., STIM is a  $\text{Ca}^{2+}$  sensor essential for  $\text{Ca}^{2+}$ -store-depletion-triggered  $\text{Ca}^{2+}$  influx, *Curr. Biol.* 15 (2005) 1235–1241.
- [9] M. Vig, C. Peinelt, A. Beck, D.L. Koomoa, D. Rabah, M. Koblan-Huberson, et al., CRACM1 is a plasma membrane protein essential for store-operated  $\text{Ca}^{2+}$  entry, *Science* 312 (2006) 1220–1223.
- [10] M. Vig, A. Beck, J.M. Billingsley, A. Lis, S. Parvez, C. Peinelt, et al., CRACM1 multimers form the ion-selective pore of the CRAC channel, *Curr. Biol.* 16 (2006) 2073–2079.
- [11] S. Feske, Y. Gwack, M. Prakriya, S. Srikanth, S.H. Puppel, B. Tanasa, et al., A mutation in Orai1 causes immune deficiency by abrogating CRAC channel function, *Nature* 441 (2006) 179–185.
- [12] M. Prakriya, S. Feske, Y. Gwack, S. Srikanth, A. Rao, P.G. Hogan, Orai1 is an essential pore subunit of the CRAC channel, *Nature* 443 (2006) 230–233.
- [13] A.V. Yeromin, S.L. Zhang, W. Jiang, Y. Yu, O. Safrina, M.D. Cahalan, Molecular identification of the CRAC channel by altered ion selectivity in a mutant of Orai, *Nature* 443 (2006) 226–229.
- [14] X. Hou, L. Pedi, M.M. Diver, S.B. Long, Crystal structure of the calcium release-activated calcium channel Orai, *Science* 338 (2012) 1308–1313.
- [15] X. Cai, Molecular evolution and functional divergence of the  $\text{Ca}(2+)$  sensor protein in store-operated  $\text{Ca}(2+)$  entry: stromal interaction molecule, *PLoS One* 2 (2007) e609.
- [16] X. Cai, Molecular evolution and structural analysis of the  $\text{Ca}(2+)$  release-activated  $\text{Ca}(2+)$  channel subunit, Orai, *J. Mol. Biol.* 368 (2007) 1284–1291.
- [17] S.S. Manji, N.J. Parker, R.T. Williams, L. van Stekelenburg, R.B. Pearson, M. Dziadek, et al., STIM1: a novel phosphoprotein located at the cell surface, *Biochim. Biophys. Acta* 1481 (2000) 147–155.
- [18] R.T. Williams, S.S. Manji, N.J. Parker, M.S. Hancock, L. Van Stekelenburg, J.P. Eid, et al., Identification and characterization of the STIM (stromal interaction molecule) gene family: coding for a novel class of transmembrane proteins, *Biochem. J.* 357 (2001) 673–685.
- [19] Y. Zhou, P. Srinivasan, S. Razavi, S. Seymour, P. Meraner, A. Gudlur, et al., Initial activation of STIM1, the regulator of store-operated calcium entry, *Nat. Struct. Mol. Biol.* 20 (2013) 973–981.
- [20] X. Yang, H. Jin, X. Cai, S. Li, Y. Shen, Structural and mechanistic insights into the activation of stromal interaction molecule 1 (STIM1), *Proc. Natl. Acad. Sci. U. S. A.* 109 (2012) 5657–5662.
- [21] M. Muik, M. Fahrner, I. Derler, R. Schindl, J. Bergsmann, I. Frischaufl, et al., A cytosolic homomerization and a modulatory domain within STIM1 C terminus determine coupling to ORAI1 channels, *J. Biol. Chem.* 284 (2009) 8421–8426.
- [22] Y. Baba, K. Hayashi, Y. Fujii, A. Mizushima, H. Watarai, M. Wakamori, et al., Coupling of STIM1 to store-operated  $\text{Ca}^{2+}$  entry through its constitutive and inducible movement in the endoplasmic reticulum, *Proc. Natl. Acad. Sci. U. S. A.* 103 (2006) 16704–16709.
- [23] G.N. Huang, W. Zeng, J.Y. Kim, J.P. Yuan, L. Han, S. Muallem, et al., STIM1 carboxyl-terminus activates native SOC, I(crac) and TRPC1 channels, *Nat. Cell Biol.* 8 (2006) 1003–1010.
- [24] M. Muik, M. Fahrner, R. Schindl, P. Stathopoulos, I. Frischaufl, I. Derler, et al., STIM1 couples to ORAI1 via an intramolecular transition into an extended conformation, *EMBO J.* 30 (2011) 1678–1689.
- [25] M.M. Wu, J. Buchanan, R.M. Luik, R.S. Lewis,  $\text{Ca}^{2+}$  store depletion causes STIM1 to accumulate in ER regions closely associated with the plasma membrane, *J. Cell Biol.* 174 (2006) 803–813.
- [26] P.B. Stathopoulos, G.Y. Li, M.J. Plevin, J.B. Ames, M. Ikura, Stored  $\text{Ca}^{2+}$  depletion-induced oligomerization of stromal interaction molecule 1 (STIM1) via the EF–SAM region: an initiation mechanism for capacitive  $\text{Ca}^{2+}$  entry, *J. Biol. Chem.* 281 (2006) 35855–35862.
- [27] P.B. Stathopoulos, L. Zheng, G.-Y. Li, M.J. Plevin, M. Ikura, Structural and mechanistic insights into STIM1-mediated initiation of store-operated calcium entry, *Cell* 135 (2008) 110–122.
- [28] L. Zheng, P.B. Stathopoulos, G.Y. Li, M. Ikura, Biophysical characterization of the EF-hand and SAM domain containing  $\text{Ca}^{2+}$  sensory region of STIM1 and STIM2, *Biochem. Biophys. Res. Commun.* 369 (2008) 240–246.
- [29] L. Zheng, P.B. Stathopoulos, R. Schindl, G.-Y. Li, C. Romanin, M. Ikura, Auto-inhibitory role of the EF–SAM domain of STIM proteins in store-operated calcium entry, *Proc. Natl. Acad. Sci. U. S. A.* 108 (2011) 1337–1342.
- [30] Y. Furukawa, S. Teraguchi, T. Ikegami, O. Dagliyan, L. Jin, D. Hall, et al., Intrinsic disorder mediates cooperative signal transduction in STIM1, *J. Mol. Biol.* 426 (2014) 2082–2097.
- [31] Y. Huang, Y. Zhou, H.C. Wong, Y. Chen, Y. Chen, S. Wang, et al., A single EF-hand isolated from STIM1 forms dimer in the absence and presence of  $\text{Ca}^{2+}$ , *FEBS J.* 276 (2009) 5589–5597.
- [32] P.B. Stathopoulos, L. Zheng, M. Ikura, Stromal interaction molecule (STIM) 1 and STIM2 calcium sensing regions exhibit distinct unfolding and oligomerization kinetics, *J. Biol. Chem.* 284 (2009) 728–732.
- [33] P.B. Stathopoulos, R. Schindl, M. Fahrner, L. Zheng, G.M. Gasmi-Seabrook, M. Muik, et al., STIM1/Orai1 coiled-coil interplay in the regulation of store-operated calcium entry, *Nat. Commun.* 4 (2013) 2963.
- [34] R.M. Luik, M.M. Wu, J. Buchanan, R.S. Lewis, The elementary unit of store-operated  $\text{Ca}^{2+}$  entry: local activation of CRAC channels by STIM1 at ER-plasma membrane junctions, *J. Cell Biol.* 174 (2006) 815–825.
- [35] M.K. Korzeniowski, M.A. Popovic, Z. Szentepekey, P. Varnai, S.S. Stojilkovic, T. Balla, Dependence of STIM1/Orai1-

- mediated calcium entry on plasma membrane phosphoinositides, *J. Biol. Chem.* 284 (2009) 21027–21035.
- [36] C.M. Walsh, M. Chvanov, L.P. Haynes, O.H. Petersen, A.V. Tepikin, R.D. Burgoyne, Role of phosphoinositides in STIM1 dynamics and store-operated calcium entry, *Biochem. J.* 425 (2010) 159–168.
- [37] N. Calloway, T. Owens, K. Corwith, W. Rodgers, D. Holowka, B. Baird, Stimulated association of STIM1 and Orai1 is regulated by the balance of PtdIns(4,5)P<sub>2</sub> between distinct membrane pools, *J. Cell Sci.* 124 (2011) 2602–2610.
- [38] J. Liou, M. Fivaz, T. Inoue, T. Meyer, Live-cell imaging reveals sequential oligomerization and local plasma membrane targeting of stromal interaction molecule 1 after  $\text{Ca}^{2+}$  store depletion, *Proc. Natl. Acad. Sci. U. S. A.* 104 (2007) 9301–9306.
- [39] C.Y. Park, P.J. Hoover, F.M. Mullins, P. Bachhawat, E.D. Covington, S. Raunser, et al., STIM1 clusters and activates CRAC channels via direct binding of a cytosolic domain to Orai1, *Cell* 136 (2009) 876–890.
- [40] J.P. Yuan, W. Zeng, M.R. Dorwart, Y.J. Choi, P.F. Worley, S. Mualem, SOAR and the polybasic STIM1 domains gate and regulate Orai channels, *Nat. Cell Biol.* 11 (2009) 337–343.
- [41] Y. Zhou, S. Mancarella, Y. Wang, C. Yue, M. Ritchie, D.L. Gill, et al., The short N-terminal domains of STIM1 and STIM2 control the activation kinetics of Orai1 channels, *J. Biol. Chem.* 284 (2009) 19164–19168.
- [42] J. Zhu, X. Lu, Q. Feng, P.B. Stathopoulos, A charge-sensing region in the stromal interaction molecule 1 luminal domain confers stabilization-mediated inhibition of SOCE in response to S-nitrosylation, *J. Biol. Chem.* 293 (2018) 8900–8911.
- [43] H. Ishida, H.J. Vogel, EF-hand proteins, in: R.H. Kretsinger, V.N. Uversky, E.A. Permyakov (Eds.), *Encyclopedia of Metalloproteins*, Springer New York, New York, NY, 2013, pp. 766–775.
- [44] C.B. Marshall, T. Nishikawa, M. Osawa, P.B. Stathopoulos, M. Ikura, Calmodulin and STIM proteins: two major calcium sensors in the cytoplasm and endoplasmic reticulum, *Biochem. Biophys. Res. Commun.* 460 (2015) 5–21.
- [45] A.C. da Silva, J. Kendrick-Jones, F.C. Reinach, Determinants of ion specificity on EF-hands sites. Conversion of the  $\text{Ca}^{2+}/\text{Mg}^{2+}$  site of smooth muscle myosin regulatory light chain into a  $\text{Ca}(2+)$ -specific site, *J. Biol. Chem.* 270 (1995) 6773–6778.
- [46] Z. Grabarek, Structural basis for diversity of the EF-hand calcium-binding proteins, *J. Mol. Biol.* 359 (2006) 509–525.
- [47] J.L. Gifford, M.P. Walsh, H.J. Vogel, Structures and metal-ion-binding properties of the  $\text{Ca}^{2+}$ -binding helix-loop-helix EF-hand motifs, *Biochem. J.* 405 (2007) 199–221.
- [48] S.R. Martin, J.F. Maune, K. Beckingham, P.M. Bayley, Stopped-flow studies of calcium dissociation from calcium-binding-site mutants of *Drosophila melanogaster* calmodulin, *Eur. J. Biochem.* 205 (1992) 1107–1114.
- [49] L. Gui, J. Zhu, X. Lu, S.M. Sims, W.Y. Lu, P.B. Stathopoulos, et al., S-nitrosylation of STIM1 by neuronal nitric oxide synthase inhibits store-operated  $\text{Ca}(2+)$  entry, *J. Mol. Biol.* 430 (2018) 1773–1785.
- [50] B.J. Hawkins, K.M. Irrinki, K. Mallilankaraman, Y.C. Lien, Y. Wang, C.D. Bhanumathy, et al., S-glutathionylation activates STIM1 and alters mitochondrial homeostasis, *J. Cell Biol.* 190 (2010) 391–405.
- [51] Y.J. Choi, Y. Zhao, M. Bhattacharya, P.B. Stathopoulos, Structural perturbations induced by Asn131 and Asn171 glycosylation converge within the EFSAM core and enhance stromal interaction molecule-1 mediated store operated calcium entry, *Biochim. Biophys. Acta* 1864 (2017) 1054–1063.
- [52] M. Ikura, J.B. Ames, Genetic polymorphism and protein conformational plasticity in the calmodulin superfamily: two ways to promote multifunctionality, *Proc. Natl. Acad. Sci. U. S. A.* 103 (2006) 1159–1164.
- [53] P.B. Stathopoulos, M. Ikura, Structure and function of endoplasmic reticulum STIM calcium sensors, *Curr. Top. Membr.* 71 (2013) 59–93.
- [54] D.W.A. Buchan, D.T. Jones, The PSIPRED protein analysis workbench: 20 years on, *Nucleic Acids Res.* 47 (2019) W402–W407.
- [55] A. Gudlur, A.E. Zeraik, N. Hirve, V. Rajanikanth, A.A. Bobkov, G. Ma, et al., Calcium sensing by the STIM1 ER-luminal domain, *Nat. Commun.* 9 (2018) 4536.
- [56] X. Yan, J. Xing, C. Lorin-Nebel, A.Y. Estevez, K. Nehrke, T. Lamitina, et al., Function of a STIM1 homologue in *C. elegans*: evidence that store-operated  $\text{Ca}^{2+}$  entry is not essential for oscillatory  $\text{Ca}^{2+}$  signaling and ER  $\text{Ca}^{2+}$  homeostasis, *J. Gen. Physiol.* 128 (2006) 443–459.
- [57] C. Lorin-Nebel, J. Xing, X. Yan, K. Strange, CRAC channel activity in *C. elegans* is mediated by Orai1 and STIM1 homologues and is essential for ovulation and fertility, *J. Physiol.* 580 (2007) 67–85.
- [58] S. Gao, Y. Fan, L. Chen, J. Lu, T. Xu, P. Xu, Mechanism of different spatial distributions of *Caenorhabditis elegans* and human STIM1 at resting state, *Cell Calcium* 45 (2009) 77–88.
- [59] T.C. Terwilliger, P.D. Adams, R.J. Read, A.J. McCoy, N.W. Moriarty, R.W. Grosse-Kunstleve, et al., Decision-making in structure solution using Bayesian estimates of map quality: the PHENIX AutoSol wizard, *Acta Crystallogr. D Biol. Crystallogr.* 65 (2009) 582–601.
- [60] P.D. Adams, P.V. Afonine, G. Bunkoczi, V.B. Chen, I.W. Davis, N. Echols, et al., PHENIX: a comprehensive Python-based system for macromolecular structure solution, *Acta Crystallogr. D Biol. Crystallogr.* 66 (2010) 213–221.
- [61] P. Emsley, K. Cowtan, Coot: model-building tools for molecular graphics, *Acta Crystallogr. D Biol. Crystallogr.* 60 (2004) 2126–2132.
- [62] G.N. Murshudov, A.A. Vagin, E.J. Dodson, Refinement of macromolecular structures by the maximum-likelihood method, *Acta Crystallogr. D Biol. Crystallogr.* 53 (1997) 240–255.
- [63] J.B. Ames, K.B. Hendricks, T. Strahl, I.G. Huttner, N. Hamasaki, J. Thorner, Structure and calcium-binding properties of Frq1, a novel calcium sensor in the yeast *Saccharomyces cerevisiae*, *Biochemistry* 39 (2000) 12149–12161.
- [64] L.E. Kay, P. Keifer, T. Saarinen, Pure absorption gradient enhanced heteronuclear single quantum correlation spectroscopy with improved sensitivity, *J. Am. Chem. Soc.* 114 (1992) 10663–10665.
- [65] L.E. Kay, M. Ikura, R. Tschudin, A. Bax, 3-Dimensional triple-resonance NMR-spectroscopy of isotopically enriched proteins, *J. Magn. Reson.* 89 (1990) 496–514.
- [66] A.C. Wang, P.J. Lodi, J. Qin, G.W. Vuister, A.M. Gronenborn, G.M. Clore, An efficient triple-resonance

- experiment for proton-directed sequential backbone assignment of medium-sized proteins, *J. Magn. Reson. B* 105 (1994) 196–198.
- [67] S. Grzesiek, A. Bax, Amino acid type determination in the sequential assignment procedure of uniformly  $^{13}\text{C}/^{15}\text{N}$ -enriched proteins, *J. Biomol. NMR* 3 (1993) 185–204.
- [68] F. Delaglio, S. Grzesiek, G.W. Vuister, G. Zhu, J. Pfeifer, A. Bax, NMRPipe: a multidimensional spectral processing system based on UNIX pipes, *J. Biomol. NMR* 6 (1995) 277–293.
- [69] N.I. Kirby, E.F. DeRose, R.E. London, G.A. Mueller, NvAssign: protein NMR spectral assignment with NMRView, *Bioinformatics* 20 (2004) 1201–1203.
- [70] L.E. Kay, D.A. Torchia, A. Bax, Backbone dynamics of proteins as studied by  $^{15}\text{N}$  inverse detected heteronuclear NMR spectroscopy: application to staphylococcal nuclease, *Biochemistry* 28 (1989) 8972–8979.
- [71] N.E. Hafsa, D. Arndt, D.S. Wishart, CSI 3.0: a web server for identifying secondary and super-secondary structure in proteins using NMR chemical shifts, *Nucleic Acids Res.* 43 (2015) W370–W377.